Hyperspectral Oblique Plane Microscopy

Ke Guo, Konstantinos Kalyviotis, Periklis Pantazis, Christopher J Rowlands

Abstract

A rapid, efficient 3D-resolved hyperspectral microscope is presented. Able to switch between hyperspectral and normal imaging modes in seconds without realignment, it is built around a commercial inverted microscope frame for ease-of-use. Performance is demonstrated on a variety of samples; utility is shown by performing highly-multiplexed fluorescence microscopy, and the sensitivity and resolution is highlighted by rapidly taking spontaneous Raman maps of micro-plastics and zebrafish embryos.

1 Main

Hyperspectral microscopy enhances and enables techniques as diverse as absorbance[1], fluorescence[2], profilometry[3, 4], Raman scattering[5] and Brillouin scattering[6] but data are typically captured slowly, by focussing at a point on the sample and taking spectra one at a time. Light-sheet microscopy (LSM, in which an orthogonal microscope objective projects a thin beam or plane through the primary microscope objective's focal plane) can speed this up by elongating the focus and recording spectra from all points along it[7], but suffers from difficulties with sample mounting geometries. In some cases there isn't enough room between the two objectives to place the sample, or the primary objective may have to image through a tilted coverslip, introducing significant optical aberrations. Approaches have been taken to apply wavefront shaping to overcome these aberrations[8, 9], but this can be complex and expensive, focussing or moving the sample can be difficult, and in the case of commercial solutions can be difficult to adapt or modify. Hyperspectral light-sheet microscopes have therefore been limited to dual-objective designs until now[10, 11, 12, 13].

To overcome these shortcomings we present a single-objective epi-illumination hyperspectral light sheet microscope, λ-OPM, which carries the advantages of LSM while resolving the sample mounting complications. It is based on an oblique-plane microscope design[14]; the use of a single microscope objective makes it compatible with most established sample formats, as well as commercial accessories such as stagetop incubators. Moreover, unlike some open top light-sheet systems, λ-OPM does not require compensation for the strong optical aberrations that result from imaging through a coverslip at a pronounced angle. The design features will be discussed, and hyperspectral imaging performance assessed. The full sensitivity and spectral resolution of the system will be demonstrated by resolving five overlapping fluorescence spectra within a ∼100 nm bandwidth, in addition to taking 3D-resolved Raman spectra from both a series of microplastics as well as a live zebrafish embryo.

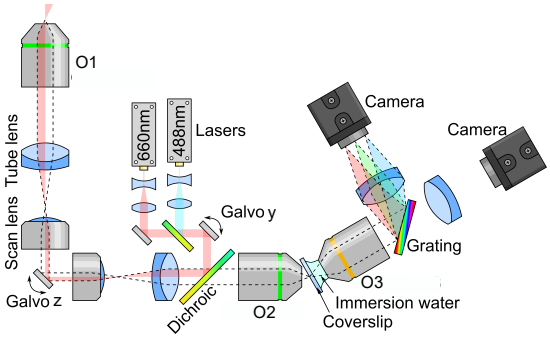

Figure 1: Optical diagram. Light from one of two lasers (488 nm or 660 nm) is expanded to ~ 0.5 mm diameter before being brought to a focus at the image plane of a microscope. The focus can be scanned anywhere in the image plane using two orthogonal galvanometric mirrors (Galvo y and Galvo z), which are made conjugate to each other using a 4f lens relay made from a scan lens and tube lens. This image is relayed to the sample with a tube lens and microscope objective (O1). Because the laser illumination passes close to the edge of the system aperture, the sample is illuminated by an oblique, weakly-focused beam. The light emitted from the sample is then imaged back through the optical system, through the dichroic mirror and into a second microscope objective (O2) where it forms a virtual image with a magnification equal to the refractive index of the sample ($\sim$1.33). A third objective (O3) then images this tilted plane onto a camera via a tube lens. For hyperspectral imaging a grating is placed in the optical path to disperse the light from the illuminated line by wavelength, recording an optical spectrum for each illuminated point. The grating can be replaced with another filter cube containing a dichroic mirror and two bandpass filters for more conventional two-colour imaging.

2 Results

2.1 Design of λ-OPM

The system design can be seen in Fig. 1. It is based on an oblique plane microscope design; a laser beam is projected through the sample at an oblique angle, and emission light (such as fluorescence, Raman scattering or Brillouin scattering) is captured by the same objective. The image of this tilted plane is formed using a second microscope objective, and a third objective is then used to compensate for the tilt, by placing the whole tilted plane within its depth of focus. The exact components used for the instrument are detailed in the Methods.

λ-OPM incorporates a grating into the infinity path of the third objective, turning it into a modest spectrometer, with an entrance slit defined by the image of the obliquely-projected laser beam. In conventional imaging mode the system has a field of view of 500 µm × 400 µm with a measured resolution of 650 nm laterally and 3400 nm axially (FWHM) within the centre $\sim$ 250µm×250 µm of the field of view; image quality is degraded slightly for objects located deeper within the sample (See Supplementary Section 2.2). In hyperspectral imaging mode, the Y axis is used as a spectral axis, providing a spectral range of approximately $\sim$200 nm. This can be adjusted either by manually adjusting the grating tilt or by moving the laser beam position with Galvo y. The vertical resolution is approximately 10-20 µm from the centre to the sides (FWHM) as

determined by the laser beam width (see Supplementary section 2.2 and Supplementary Fig. 2(a)).

2.2 λ-OPM can resolve numerous overlapping fluorescence spectra

A major virtue of λ-OPM is the ability to image samples containing a large number of different dyes with overlapping emission spectra. To demonstrate this capability, we successfully resolved five very similar fluorophores in a sample consisting of an emulsion of water droplets in an organic solution (sample preparation details available in the Methods). Each droplet contains one of five water-soluble quantum dots with nominal emission maxima near 525 nm, 550 nm, 575 nm, 600 nm and 630 nm, as shown in Figure 2(a). Figure 2(b) shows one example of a single spectrally-resolved line (i.e. an x-λ plot) of this sample (with the image of the laser beam deconvolved). Even in this one line, four regimes with distinct spectra can be observed between $x = 180$ µm to $x = 500$ µm, corresponding to four droplets containing different quantum dots. The broad spectrum on the left side (from $x = 0$ to $x = 180$ µm) results from a large droplet at the bottom of the sample which itself results from the fusion of several droplets containing different quantum dots.

To identify the quantum dots in the droplets, we fit the deconvolved measured spectra at different positions as a weighted sum of the five individual quantum dot spectra. Figure 2(c) shows the five spectral components separated by the fit, as a function of position as the sample stage scanned in the y direction. All five maps exhibit distinct spatial distributions in the form of tightly packed droplets. Most droplets (except the bottom large droplet) have one dominating colour and the accuracy of the spectrum separation depends on the spatial and spectral overlap. Large droplets containing the 525 nm and 600 nm quantum dots can be well isolated from other colours despite the significant spectral overlap. A zoomed in image in Figure 2(d) shows that features as small as 10 µm can be resolved in both x and y. Similar results can be obtained for different positions in z by scanning the laser beam using the mirror Galvo z as shown in Figure 2(e). 3D hyperspectral imaging of the sample can be achieved by combining the sample scan in y and laser scan in z.

2.3 Speeding up Raman mapping several hundredfold

Apart from the capability of unmixing different fluorescent spectra, λ-OPM also features a high sensitivity, which is ideal for fast Raman scattering measurements. Raman scattering measurements are challenging due to the weak Raman-scattering cross-section, the extremely strong Rayleigh-scattered signal, and the influence of background fluorescence. The high photon-efficiency and absence of out-of-focus illumination in λ-OPM effectively mitigate these issues. To demonstrate this functionality, we measure the Raman spectra of different polymer micro-particles and thereby determine their composition.

The sample measured was a mixture of polymer microparticles embedded in agarose gel; these microparticles were composed of either polystyrene-co-divinylbenzene (PS, 6-10 µm), polymethylmethacrylate (PMMA, 6-10 µm) or polyamide-nylon6 (PA6, 5-50 µm). When a particle entered the laser beam, its Raman spectrum appeared as a series of bands with the vertical positions corresponding to the peaks of the spectrum. Fig. 3(a) shows an example of a cropped hyperspectral Raman scattering image with no deconvolution applied as most of the particles were smaller than the laser beam. Two different particles can be clearly identified in the middle of the image with their different Raman spectra (Fig. 3(c)) corresponding to PS and PMMA. Apart from the Raman peaks, a broad fluorescence spectrum can be observed on the left, which results from the bottom of the 35 mm glass-bottomed dish holding the gel.

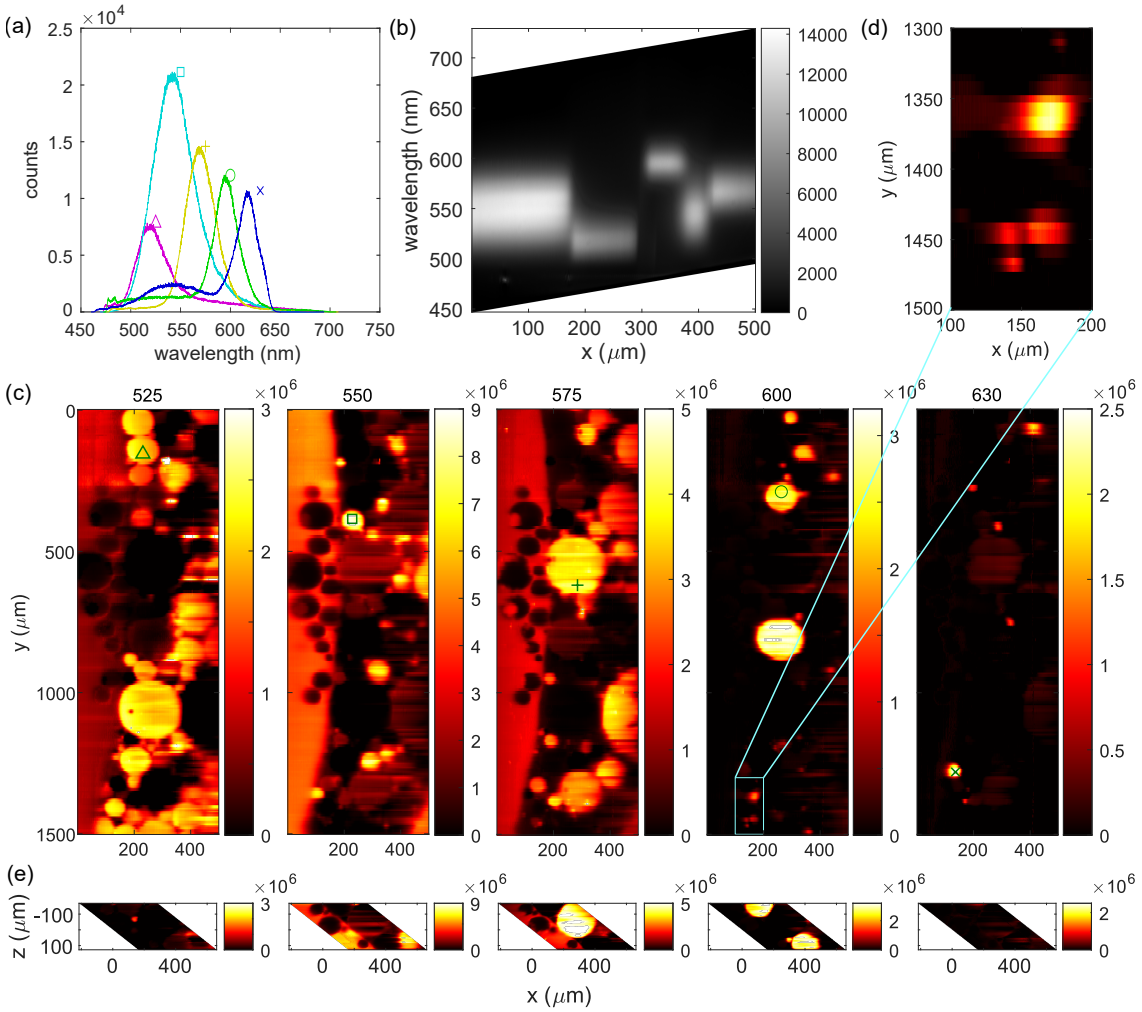

Figure 2: (a) Emission spectra of five quantum dot droplets, obtained from vertical cuts through hyperspectral images and sharpened by deconvolving the laser beam profile. The side peak of the 630 nm quantum dot (blue) at 550 nm is a result of background fluorescence from nearby droplets. (b) A hyperspectral image (with the laser beam image deconvolved) of quantum dot droplets showing five droplets each with different emission spectra. (c,e) Proportion of each quantum dot spectrum as a function of position, obtained by fitting each deconvolved spectrum as a weighted sum of the five individual quantum dot spectra. (c) Image formed by scanning the sample stage in y. (e) Image formed by scanning the laser beam in z. The measured spectra at the markers are plotted in (a). (d) A zoomed-in section of (c) (600 nm only, with colour bar re-scaled). Exposure time: 200 ms per frame, laser power: 5 mW.

By scanning the sample stage in y and the laser beam in z, the Raman spectra of particles in

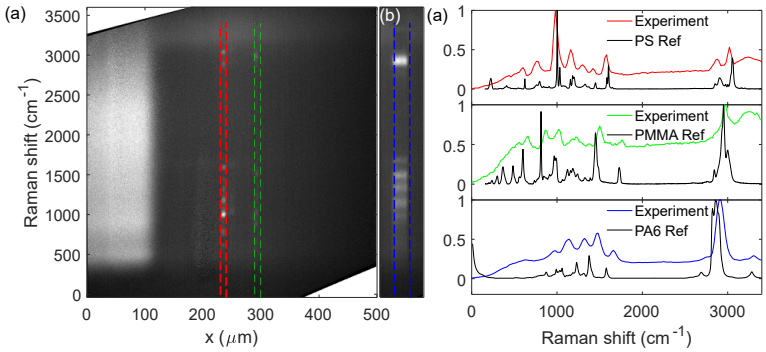

Figure 3: (a) A hyperspectral image of the Raman scattering from a mixture of PS, PMMA and PA6 in Agarose, which shows two distinctly different spectra of PS and PMMA respectively near $x = 250$ μm. Exposure time: 0.5 s, laser power: 800 mW. (b) A cropped hyperspectral image from the same sample showing the Raman spectrum of a PA6 particle. (c) Raman spectra (normalized, leveled by subtracting a background spectrum, and averaged in the x direction) within the dashed lines in (a-b), in comparison with the Raman spectra of PS, PMMA and PA6 obtained from Ref. [15, 16].The grating parameters are set to match the references.

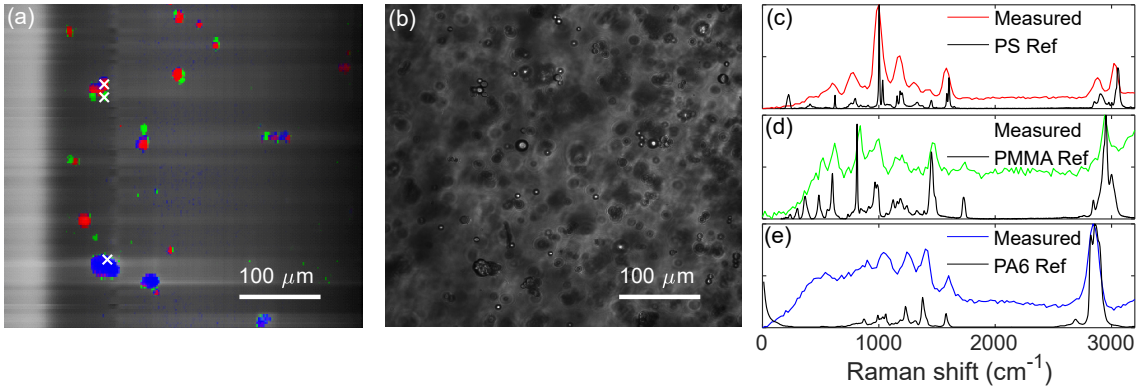

Figure 4: (a) A false colour Raman scattering image constructed from 198 scan locations in the y direction, with the type material at each position identified using CNN. The brightness of the image is scaled with a gradient in the x direction to compensate for the laser intensity reduction as it passed the sample. Red: PS, green: PMMA, blue: PA6, grey: agarose or dish. Exposure time: 0.5 s per line, laser power: 800 mW. The data was binned every 10 pixels in the x direction. (b) A (Rayleigh) scattering image of the same sample area illuminated by a white light torch from above the sample stage. (c-e) Measured Raman spectra at the 3 marked pixels in (a), showing good correspondence to the reference spectra of the corresponding polymers identified by the CNN.

a 3D volume can be obtained for mapping the location and composition of different particles. For improved signal to noise ratio, pixels were binned in groups of 10 in the x direction, and pixels outside the middle 350 μm of the image cropped out, yielding a total of approximately 180 spectra per line. We use a convolutional neural network (CNN) [17, 18] to classify the different polymers. The training and test data were measured from three samples, each with one type of polymer particle in agarose, along with one sample containing pure agarose for the spectra of agarose and any residual signal from the glass-bottomed dish. 14982 Raman spectra were measured, with approximately 3000 spectra for each of the five classes. We used 80 % of the measured spectra for training, and 20 % for testing. The resulting model has an accuracy of over 98 % for both the training and test data.

For each spectrum, the CNN outputs a set of five scores corresponding to the 3 polymers, agarose and glass-bottomed dish, which we use to classify the Raman spectra at different locations. Using the five scores as weights, we distribute the total scattering intensity into the RGB channels of the image, with PS for red, PMMA for green, PA6 for blue, and agarose or dish (sum of the two divided by 3) for all three channels (i.e. grey). Fig. 4(b) shows a map of 201 stage locations in the y direction. Compared to a white light scattering-contrast image of the same area in Fig. 4(b), the map captures not only the location and shape of most of the particles on the focal plane with a higher contrast, but also the polymer type of each particle. The Raman spectra of the three marked pixels in Fig. 4(c) show clear correspondence with the reference spectra, verifying the material classifications.

2.4 Rapid in vivo Raman imaging of a live zebrafish embryo

To further demonstrate the Raman imaging capacity of λ-OPM, we measured the 2D-resolved Raman spectra of a living but wounded zebrafish embryo, using the same instrument configuration as for the previous Raman imaging experiments. The sample was a wild-type (WT/AB) embryo at 3 days post-fertilization. The embryo was wounded by making a single incision using a pair of forceps in the dorsal myotome opposite to the anal pore as illustrated in Fig. 5(a). The measurements were conducted approximately 4 hours after the wound was made. Fig. 5(b) shows exemplar Raman spectra at three different regions of the fish featuring different molecule compositions. The spectrum at the muscle (blue) contains peaks near 970 cm^{-1}, 1300 cm^{-1}, 1640 cm^{-1}, 2930 cm^{-1}, and 3250 cm^{-1} (from water), agreeing with typically measured Raman spectra of proteins and lipids in zebrafish [19]. In addition to these peaks, the wound spectrum (red) has two features near 1160 cm^{-1} and 1500 cm^{-1} (red dashed lines). They correspond with the Raman spectrum of carotenoids (conjugated C–C=C–C stretch) commonly observed in the blood. The spectrum taken from the yolk (green) exhibits strong autofluorescence signal as well as a suppression of the water peak, indicating a higher ratio of organic molecules.

Based on the above observation, we identify 3 types of molecules in the fish (i.e. collagen, carotenoids, and lipids) by comparing the prominence of the corresponding spectral peaks as detailed in Supplementary section 3.4. Using 301 hyperspectral frames at different sample positions in y, we map the distribution of collagen, carotenoids, and lipids in Fig. 5(c-f). The collagen signal is distributed in the whole body and mostly in the muscles. The carotenoid can be found in the gut, the bone and the wound. The lipid signal is distributed in the whole body and more prominently in the yolk. The wound caused a clear increase of carotenoid, and a reduction of collagen, which agrees with similar work [19].

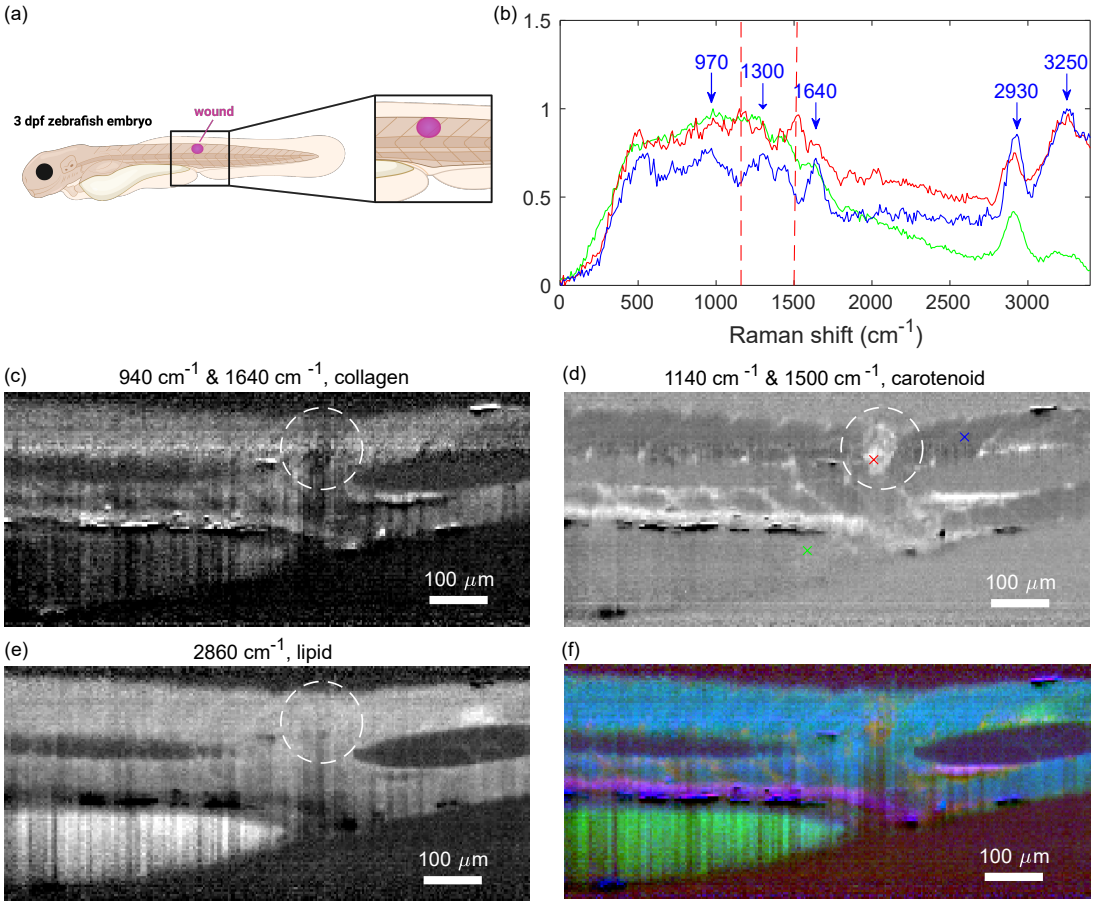

Figure 5: (a) An illustration of the investigated zebrafish embryo showing the estimated image area and wound location. (b) Example spectra (normalized) obtained from the back muscle (blue), the wound (red) and the yolk (green) of the fish. The blue arrows mark the different spectrum peaks corresponding to Raman peaks of proteins and lipids. The red dashed lines indicate the two additional peaks expected from carotenoids. (c-e) Distributions of (c) collagen, (d) carotenoids, and (e) lipids obtained from 301 hyperspectral images. The crosses indicate the locations corresponding to the spectra in (b). (f) A false colour image combining (c-e) in the blue, red, and green channels respectively. The circles indicate the estimated wound location. Laser power: 600 mW, exposure time: 2 s per frame, pixel size: 3.9 $\mu m \times 5$ μm.

3 Discussion

λ-OPM was designed from the start to achieve unprecedented hyperspectral volumetric imaging performance (speed, throughput and sensitivity) without compromising the familiarity, flexibility, ease of use and compatibility with third-party components that a commercial microscope frame provides. The system achieves its performance through careful component choice; the 0.93 theoretical collection numerical aperture, low-noise cameras and use of high-performance anti-reflection coatings help maintain image brightness despite the grating dispersion and significant number of optical surfaces present in the system. It is this throughput and sensitivity which gives rise to the high imaging rates (∼200 ms per line for fluorescence microscopy, 0.5 - 2 s per line for biological Raman imaging). The exposure value for fluorescence microscopy is conservative and can be decreased significantly for brighter samples.

Our design permits the user to change from two-channel to hyperspectral imaging without needing to realign. This was done by creating a filter cube insert containing a grating on a custom kinematic mount. The grating was tilted such that Rayleigh-scattered light did not strike the camera sensor; exact construction details can be found in Supplementary Section 3. For two-channel imaging the filter cube can be replaced by one containing a dichroic and two emission filters. Other key design features are the ability to rapidly scan the excitation beam using a galvanometric mirror (for use when rapidly capturing hyperspectral depth maps as exemplified in Figure 2(e)), and a custom water-immersion chamber for the tilted OPM objective. This water chamber is more complex to implement than a solid immersion lens[20], but offers greater flexibility, larger field of view and the opportunity to use lenses with a broader range of design wavelengths. Depending on which objective lens is chosen this can result in significant cost savings as well.

In terms of utility, the ability to multiplex five fluorophores within a ∼100 nm bandwidth is extremely difficult to achieve using conventional bandpass filters; examination of Figure 2(a) shows that even if infinitely-sharp bandpass filters were available there would be no band that avoids significant spectral crosstalk. While we optimized λ-OPM for a 3000 cm^{-1} Raman spectral range, substituting the 300 lp/mm grating would theoretically allow for a much greater spectral range in the visible region of the electromagnetic spectrum, allowing fifteen or more different fluorescence emission spectra to be distinguished in the range 450-750nm, for example.

While λ-OPM is flexible and is compatible with almost all conventional microscopy samples, there are of course limitations. Like all light-sheet systems there is an increased sensitivity to sample scattering compared to confocal and multiphoton microscopy; when performing hyperspectral imaging this scattering can start to degrade the spectral resolution as well (since the spectrum is convolved with the width of the excitation profile). In practice, the effect is manageable and deconvolution can be used to recover even fine details in biological Raman spectra. As case in point, we have successfully imaged almost 400 μm into a live zebrafish embryo, confirming that this sensitivity does not preclude practical biological Raman imaging.

Another minor limitation is the sheared image on the camera which results from the tilt of the grating. This tilt is needed to project the first diffraction order onto the camera (and not the zeroth order), but unfortunately causes a modest degree of image distortion, and the shear means the spectral range varies as a function of position along the light sheet. This can theoretically be avoided with a tranmission-mode grism[21], although this comes at the cost of increased budget, mounting concerns due to size, and reduced system aperture.

In summary, we have introduced a first ever single-objective hyperspectral light sheet microscope, λ-OPM. As a light sheet technique it addresses common shortcomings in hyperspectral

imaging, such as high photon loss and low speed, while minimizing out-of-focus photodamage and background. Moreover, it is free from the sample mounting complications of conventional light sheet systems. The utility of high-throughput hyperspectral imaging was demonstrated by successfully imaging five different fluorophores with peak maxima spaced by less than ∼30 nm, by performing spontaneous Raman mapping of polymer microspheres within two minutes, and taking a 900 $\mu m \times 400$ μm spontaneous Raman map of the tail of a live zebrafish embryo in 12 minutes.

References

[1] M. J. Baker, J. Trevisan, P. Bassan, R. Bhargava, H. J. Butler, K. M. Dorling, P. R. Fielden, S. W. Fogarty, N. J. Fullwood, K. A. Heys, C. Hughes, P. Lasch, P. L. Martin-Hirsch, B. Obinaju, G. D. Sockalingum, J. Sule-Suso, R. J. Strong, M. J. Walsh, B. R. Wood, P. Gardner, and F. L. Martin, "Using fourier transform ir spectroscopy to analyze biological materials," *NATURE PROTOCOLS*, vol. 9, pp. 1771–1791, AUG 2014.

[2] M. Dickinson, G. Bearman, S. Tille, R. Lansford, and S. Fraser, "Multi-spectral imaging and linear unmixing add a whole new dimension to laser scanning fluorescence microscopy," *BIOTECHNIQUES*, vol. 31, pp. 1272+, DEC 2001.

[3] M. BROWNE, O. AKINYEMI, and A. BOYDE, "Confocal surface profiling utilizing chromatic aberration," *SCANNING*, vol. 14, pp. 145–153, MAY-JUN 1992.

[4] S. Cha, P. Lin, L. Zhu, P. Sun, and Y. Fainman, "Nontranslational three-dimensional profilometry by chromatic confocal microscopy with dynamically configurable micromirror scanning," *APPLIED OPTICS*, vol. 39, pp. 2605–2613, JUN 1 2000.

[5] J.-X. Cheng and X. S. Xie, "Vibrational spectroscopic imaging of living systems: An emerging platform for biology and medicine," *SCIENCE*, vol. 350, NOV 27 2015.

[6] G. Scarcelli and S. H. Yun, "Confocal brillouin microscopy for three-dimensional mechanical imaging," *NATURE PHOTONICS*, vol. 2, pp. 39–43, JAN 2008.

[7] J. Huisken, J. Swoger, F. D. Bene, J. Wittbrodt, and E. H. K. Stelzer, "Optical sectioning deep inside live embryos by selective plane illumination microscopy," *Science*, vol. 305, no. 5686, pp. 1007–1009, 2004.

[8] K. Elgass, D. Hartmann, J. Siebenmorgen, T. Kalkbrenner, and K. Weisshart, "Breakthrough instruments and products: Lattice lightsheet 7-non-invasive imaging of the subcellular dynamics of life," *REVIEW OF SCIENTIFIC INSTRUMENTS*, vol. 92, OCT 1 2021.

[9] N. Vladimirov, F. Preusser, J. Wisniewski, Z. Yaniv, R. A. Desai, A. Woehler, and S. Preibisch, "Dual-view light-sheet imaging through a tilted glass interface using a deformable mirror," *BIOMEDICAL OPTICS EXPRESS*, vol. 12, pp. 2186–2203, APR 1 2021.

[10] I. Barman, K. M. Tan, and G. P. Singh, "Optical sectioning using single-plane-illumination raman imaging," *JOURNAL OF RAMAN SPECTROSCOPY*, vol. 41, pp. 1099–1101, OCT 2010.

[11] W. Jahr, B. Schmid, C. Schmied, F. O. Fahrbach, and J. Huisken, "Hyperspectral light sheet microscopy," *NATURE COMMUNICATIONS*, vol. 6, SEP 2015.

[12] S. Crombez, P. Leclerc, C. Ray, and N. Ducros, "Computational hyperspectral light-sheet microscopy," *OPTICS EXPRESS*, vol. 30, pp. 4856–4866, FEB 14 2022.

[13] W. Mueller, M. Kielhorn, M. Schmitt, J. Popp, and R. Heintzmann, "Light sheet raman microspectroscopy," *OPTICA*, vol. 3, pp. 452–457, APR 20 2016.

[14] C. Dunsby, "Optically sectioned imaging by oblique plane microscopy," *Opt. Express, OE*, vol. 16, pp. 20306–20316, Dec. 2008. Publisher: Optica Publishing Group.

[15] "RamanLife." `https://ramanlife.com/`.

[16] "PublicSpectra." `https://publicspectra.com/`.

[17] Z. Wang, W. Yan, and T. Oates, "Time series classification from scratch with deep neural networks: A strong baseline."

[18] hfawaz, "Timeseries classification from scratch." `https://keras.io/examples/timeseries/timeseries_classification_from_scratch/`.

[19] H. Høgset, C. C. Horgan, J. P. K. Armstrong, M. S. Bergholt, V. Torraca, Q. Chen, T. J. Keane, L. Bugeon, M. J. Dallman, S. Mostowy, and M. M. Stevens, "In vivo biomolecular imaging of zebrafish embryos using confocal Raman spectroscopy," *Nat Commun*, vol. 11, p. 6172, Dec. 2020. Number: 1 Publisher: Nature Publishing Group.

[20] E. Sapoznik, B.-J. Chang, J. Huh, R. J. Ju, E. V. Azarova, T. Pohlkamp, E. S. Welf, D. Broadbent, A. F. Carisey, S. J. Stehbens, K.-M. Lee, A. Marín, A. B. Hanker, J. C. Schmidt, C. L. Arteaga, B. Yang, Y. Kobayashi, P. R. Tata, R. Kruithoff, K. Doubrovinski, D. P. Shepherd, A. Millett-Sikking, A. G. York, K. M. Dean, and R. P. Fiolka, "A versatile oblique plane microscope for large-scale and high-resolution imaging of subcellular dynamics," *eLife*, vol. 9, p. e57681, Nov. 2020. Publisher: eLife Sciences Publications, Ltd.

[21] H. Matsuoka, Y. Kosai, M. Saito, N. Takeyama, and H. Suto, "Single-cell viability assessment with a novel spectro-imaging system," *JOURNAL OF BIOTECHNOLOGY*, vol. 94, pp. 299–308, APR 11 2002.